ACS OMEGA

http://pubs.acs.org/journal/acsodf

Article

One-Pot Synthesis of Nitrogen-Doped Graphene Quantum Dots and Their Applications in Bioimaging and Detecting Copper Ions in Living Cells

Xiao Liu and Bingxue Sun*

Cite This: *ACS Omega* 2023, 8, 27333−27343

Read Online

ACCESS | Metrics & More | Article Recommendations

ABSTRACT: Two natural carbon sources, glutamic acid and tyrosine, were used to fabricate strong green emission nitrogen-doped graphene quantum dots (N-GQDs) with the one-pot pyrolysis method. The morphology of the prepared GQDs has been characterized by high-resolution transmission electron microscopy, showing a well-displayed crystalline structure with a lattice spacing of 0.262 nm. X-ray photoelectron spectroscopy and Fourier transform infrared spectroscopy were used to analyze the surface functional groups and elemental composition, suggesting that the N-GQDs have active carboxylic and amino functional groups. Meanwhile, photoluminescence and ultraviolet−visible (UV−vis) spectroscopy were used to evaluate the optical properties of GQDs; the prepared N-GQDs show an excitation-dependent fluorescence behavior with a maximum excitation/emission wavelength at 460/522 nm, respectively. N-GQDs showed good photostability and the fluorescence intensity quenched about 10% after irradiating 2800 s in the experiment of time kinetic analysis. The MTT assay was utilized to assess the viability of N-GQDs; good biocompatibility with a relatively high quantum yield of 12% demonstrated the potential for serving as bioimaging agents. Besides, the selectivity study on metal ions indicates that the N-GQDs could be used in Cu^{2+} detection. The linear range is from 0.1 to 10 μM with a limit of detection of 0.06 μM. Overall, these proposed N-GQDs with one-pot synthesis showed their promising potential in cell imaging and Cu^{2+} monitoring applications involved in the biological environment.

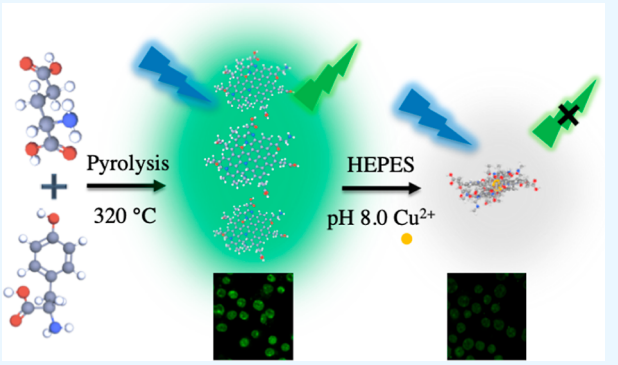

INTRODUCTION

Graphene quantum dots (GQDs) are a series of nanometer-sized (<10 nm) graphene-based fragments with unique physical, chemical, optical, and biological properties, which are potential candidates in biosensing, bioimaging, and biomedical applications.[1−6] A few decades ago, most of the bioimaging agents were organic compounds, such as fluorescein and rhodamine. However, their instinct high toxicity, low photostability, and narrow absorption cross section restrained their applications in biological and biomedical analyses.[7,8] Afterward, fluorescent nanomaterials like quantum dots were developed for use in biomedical applications.[9] Compared with traditional organic dyes, semiconducting quantum dots (QDs) showed excellent optical properties like preeminent photostability, large Stokes shift, broad absorption cross section, and low cost for scale-up production.[10] However, most metal-based QDs are cytotoxic; surface modification was a challenging situation before application in pharmaceutical or biomedical studies.

The development of GQDs has been considered as a promising resolution to break through this problem; GQDs are zero-dimensional derivatives of 2D graphene sheets in the family of carbon-based nanomaterials with excellent dispersibility, adjustable luminescent properties, and low toxicity.[11,12] The optical properties of GQDs are mainly determined by the quantum confinement effects regulated by the graphene core structure and the edge effects of surface chemical groups.[13] Therefore, it has been reported that the diversity of GQDs could be controlled and designed to be applied in different types of studies.[14,15] The synthesis of GQDs could be separated into two approaches at length: bottom-up and top-down methods.[16,17] The top-down methods could be summarized as producing GQDs from larger sized carbon-based materials, for example, acidic exfoliation splits large carbon materials through oxygen-based defects and brings oxygen-based functional groups to the surface of GQDs. The most popular route is using nitric acid or sulfuric acid to assist

Received: April 20, 2023
Accepted: July 7, 2023
Published: July 23, 2023

© 2023 The Authors. Published by American Chemical Society

in the breaking of large size carbon source, such as graphite powder, carbon fiber, or nanotube, to prepare GQDs.[18] There are also some other top-down methods like electrochemical oxidation or hydrothermal reaction.[19,20] However, most of the GQDs produced from this classical route showed low quantum yield and went through multiple purification processes.[21] The bottom-up methods are involved in some processes including carbohydrate carbonization, pyrolysis, or organic synthesis.[22−24] Pyrolysis is one of the most popular bottom-up methods and has been reported to prepare a series of blue emission GQDs in many publications.[25,26] For example, Chen's group utilized citric acid to produce GQDs by heating up to 200 °C for 30 min.[27] Doong's group designed a sulfur-doped GQD sensor by pyrolyzing citric acid and 3-mercaptosuccinic acid.[28] The carbon source of bottom-up methods is chosen from small organic molecules, such as citric acid, urea, carbohydrates, and amino acids.[29] The essential properties of GQDs relied on the carbon source molecules; for example, they could be deliberately modulated to introduce heteroatoms by choosing the decent carbon source carrying the same heteroatoms.[30] For example, Qu group used urea and thiourea to prepare S,N co-doped GQDs and applied them as visible light photocatalysts.[31] Zhu's group developed N-doped GQDs using humic acid to produce highly fluorescent GQDs for bioimaging.[32] Compared with undoped GQDs, the heteroatom-doped GQDs showed diverse properties.[33] Therefore, inspired by the previous work, we chose to use two natural amino acids to fabricate novel nitrogen-doped GQDs (N-GQDs) and validate their potential for bioimaging and biodetection.

In this project, we have successfully synthesized N-GQDs with the one-pot pyrolysis method with tyrosine and glutamic acid. The N-GQDs had a narrow distribution and emitted strong green fluorescence. Most of the GQDs prepared by pyrolysis used chain-shaped precursors for carbonization to form a hexatomic ring structure. Herein, tyrosine, as an aromatic amino acid, was chosen to prepare GQDs. The rigid benzene structure has effectively affected the pyrolysis process and changed the instinct properties to cause larger particle size distribution. The prepared N-GQDs emitted strong green fluorescence with a quantum yield of ca. 12%. In addition, the fluorescence of N-GQDs could be easily quenched in the presence of Cu^{2+}, demonstrating the potential to quantitively monitor Cu^{2+}. Besides the aqueous environment, we have also validated the N-GQDs to be applied in serum samples and in living cells. Therefore, these N-GQDs could be used for the study of bioimaging and Cu^{2+}-involved diagnostic assays.

EXPERIMENTAL SECTION

Chemicals. Tyrosine, glutamic acid, 4-(2-hydroxyethyl)-1-piperazineethanesulfonic acid (HEPES), copper sulfate, sodium hydroxide, hydrochloric acid, 3-(4,5-dimethylthiazol-2-yl)-2,5-diphenyltetrazolium bromide (MTT, $C_{18}H_{16}BrN_5S$), and fetal bovine serum (FBS) were purchased from Sigma-Aldrich Inc. Dulbecco's modified Eagle's medium (DMEM) and 4′-6-diamidino-2-phenylindole (DAPI, $C_6H_{15}N_5$) were purchased from Thermo Fisher Scientific Inc. The mouse leukemic macrophage cell line (RAW 264.7) was purchased from the American Tissue Culture Collection (ATCC). The human embryonal kidney cell line (293FT) and a sterile syringe filter (0.45 μm cellulose acetate) were obtained from Thermo Fisher Scientific Inc. All reagents were of analytical grade. All buffer solutions were prepared from ultrapure water (18 MΩ cm) produced by a Millipore Milli-Q water purification system.

Synthesis of N-GQDs. The preparation of N-GQDs was followed by a simple pyrolysis process; briefly, 0.5 g of tyrosine was thoroughly mixed with 1.5 g of glutamic acid in a glass vial. The mixture solids of two amino acids were ground first before heating up to 320 °C on a hot plate. The color of the mixture turned from white to red-brown within 1 min, indicating the formation of N-GQDs. Then, an aliquot of 10.0 mL of distilled water was added into the glass vial, and the solution was continuously stirred for 30 min. The solution was cooled down to room temperature and centrifuged at 10,000 rpm for another 30 min to remove the large particles. Finally, the supernatant was transferred into a dialysis bag (molecular weight cutoff = 1000) for 24 h against distilled water. The produced N-GQDs could be stored in room temperature for further use.

Instruments. A JEOL 2100 transmission electron microscope was utilized to obtain the particle morphology of the N-GQDs at an acceleration voltage of 200 kV. The hydrodynamic diameter and zeta potential of the N-GQDs were obtained from a Zetasizer Nano ZS. A Shimadzu FTIR-8400s spectrometer was used to collect the Fourier transform infrared (FTIR) spectra of GQDs, tyrosine, and glutamic acid. An Agilent 8453 was used to obtain the absorption spectra of GQDs, tyrosine, and glutamic acid. All the fluorescence measurements were recorded by a Shimadzu RF-6000 fluorophotometer. The excitation wavelength was set to be 460 nm, and the emission wavelength was recorded from 480 to 700 nm. The fluorescence intensity at 522 nm was chosen to determine the performance of copper detection. Both the widths of excitation and emission slits were set to be 10.0 nm. All the experiments were carried out at 25 °C. An AA-6880 atomic absorption spectrophotometer equipped with a graphite furnace was used to determine the concentrations of Cu^{2+} in FBS. X-ray photoelectron spectroscopy (XPS) was performed on a ESCALAB 250Xi XPS with a base pressure of 10^{-10} mbar. The aluminum Kα X-ray radiation was the X-ray source for excitation. The X-ray diffraction (XRD) profiles were recorded on a Rigaku D/MAX-2550 X-ray diffractometer with Cu Kα as the X-ray radiation source at 40 kV and 40 mA. A Multiskan spectrum spectrophotometer was employed to perform the MTT test for measuring the optical density at 570 nm in a dimethyl sulfoxide (DMSO) solution.

pH Effect and Photostability. The N-GQD solution was incubated under the pH condition from 3 to 12. Then, the fluorescence intensity of each N-GQD solution of different pHs was recorded. The photostability of N-GQDs was investigated by performing a time-based fluorescence collection for 2800 s. FITC was used as the control group. Besides, the zeta potential of N-GQDs was evaluated from pH 2.0 to pH 12.0 in 20 mM HEPES buffer.

Quantum Yield Measurement. Quinine sulfate in 0.1 M H_2SO_4 (QY = 0.54) was chosen as a standard for quantum yield measurement. The quantum yield of GQDs was calculated according to the following formula

$$\Phi_x = \Phi_{st}\left(\frac{\mathrm{Grad}_x}{\mathrm{Grad}_{st}}\right)\left(\frac{\eta_x^2}{\eta_{st}^2}\right)$$

Here, Φ_x is the quantum yield of GQDs. Grad is the gradient from the plot of integrated fluorescence intensity vs absorbance and η is the refractive index of the solvent (1.33

https://doi.org/10.1021/acsomega.3c02705
ACS Omega 2023, 8, 27333−27343

for water). The subscript "st" stands for the standard of quinine sulfate and "x" stands for GQDs. To minimize the reabsorption effects, absorbances of the samples were kept under 0.1 at the excitation wavelength (460 nm).

Metal Ion Selectivity Investigation. A sequence of metal ions was investigated to test the resistance of N-GQDs; the N-GQD solution was mixed with each metal ion separately including Ni^{2+}, Al^{3+}, Co^{2+}, Pb^{2+}, Cd^{2+}, Mn^{2+}, Mg^{2+}, Zn^{2+}, Fe^{3+}, Cu^{2+}, K^{+}, Sn^{2+}, Ba^{2+}, Fe^{2+}, and Na^{+}. The concentration of all the metal ions was set up to 20 μM in the final mixture solution. The fluorescence intensity of N-GQDs was recorded at 522 nm with an excitation wavelength of 460 nm.

Copper(II) Ion Detection. To investigate the sensitivity of this copper sensing fluorescent probe, an aliquot of 2.0 mL of 0.5 mg/mL N-GQDs was incubated with different concentrations of Cu^{2+} for 15 min. The concentration of Cu^{2+} ranged from 0 to 160 μM. For each concentration group, the fluorescence intensity at 522 nm was recorded at an excitation wavelength of 460 nm.

Biocompatibility of N-GQDs in Cells. The MTT assay was used to evaluate the cytotoxicity of the N-GQDs by incubating with cells at different N-GQD concentrations for 24 h. RAW 264.7 cells and 293FT cells were cultured in a DMEM cell medium in a 5% CO_2 humidified atmosphere at 37 °C for 24 h. Both of the two cell lines were rinsed with PBS buffer and then treated with different concentrations of N-GQDs (0, 10, 1, 0.1, 10^{-2}, 10^{-3}, 10^{-4}, and 10^{-5} mg/mL) for another 24 h in DMEM. After washing them to remove the physically adsorbed N-GQDs, the MTT solution (10 μL, 5.0 mg/mL) was subsequently added into each well and continuously incubated for 4 h. DMSO was added to dissolve the formed formazan violet crystals after the medium was removed. The absorbance of formazan in DMSO solution at 570 nm was detected by a microplate reader.

In Vitro Fluorescence Imaging of Cells and Copper Monitoring. Mouse leukemic macrophage cells (RAW 264.7) were chosen as a model cell to obtain fluorescence images. In general, RAW 264.7 cells were first cultured with N-GQDs at 37 °C in DMEM containing 10% FBS in a 5% CO_2 environment for 24 h. Then, RAW 264.7 cells were washed three times with PBS buffer (pH 7.4), and then an aliquot of 500 μL of 10 mg/mL GQDs (10 mM PBS buffer, pH 7.4) was added into the above cell culture plates. Afterward, the cells were incubated at 37 °C for 1 h in a 5% CO_2 environment. Finally, an aliquot of 3.0 μL of 1.0 mg/mL DAPI was used to stain the cell nucleus, and the cells were washed three times with PBS to remove the free GQDs and the excess DAPI. A Zeiss LSM-510 Meta confocal microscope was utilized to take fluorescence images of these cells after being fixed with 4% paraformaldehyde and washed with PBS.

Additionally, RAW264.7 cells were used to evaluate the feasibility of detecting copper ions in vitro. RAW264.7 cells were first seeded in 12-well plates overnight in DMEM containing 10% FBS in a 5% CO_2 environment. The cells were rinsed with PBS (10 mM) three times and then separated into three groups. One group of cells was incubated only with N-GQD (10.0 mg/mL) PBS solution, one group of cells was cultured in N-GQD (10.0 mg/mL) PBS solution and continuously added copper ions (100 μM), and the last group of cells was incubated in N-GQDs (10.0 mg/mL) and continuously added more copper ions (200 μM). All the three groups were incubated for 1 h. Subsequently, 4% paraformaldehyde was used to fix the cells, and then the cells were washed with PBS three times. Eventually, the Zeiss LSM-510 Meta confocal fluorescence microscope was used to take the fluorescence images of these cells. The fluorescence intensity detected in cells could be quantified by the cell imaging process with ImageJ software.

RESULTS AND DISCUSSION

Design and Preparation of the Highly Fluorescent N-GQDs. A superficial bottom-up approach was developed to prepare N-GQDs with glutamic acid and tyrosine together through a one-pot pyrolysis reaction. We chose to fabricate high-brightness N-GQDs with tyrosine and glutamic acid. Tyrosine and glutamic acid would assist doping nitrogen atoms to alter the intrinsic properties in the process of pyrolyzing, which leads to higher red shift emission and a relatively higher quantum yield in comparison with other bottom-up methods which used small carbon-based chain molecules as precursors shown in Table 1. Besides, two ingredients are nontoxic and inexpensive precursors involved in the process of biosynthesis of proteins, demonstrating that the routine is a one-step environment-friendly and low-cost method. Moreover, the procedure was simple and fast without the complicated purification process, which is suitable for large-scale production. The formation of N-GQDs is illustrated in Scheme 1; glutamic acid was mixed with tyrosine and then heated up to 320 °C. During the heating process, the solid mixture was first transferred into a colorless liquid and then turned into a yellow solution; eventually, it turned into a red-brown solution, indicating the formation of N-GQDs. The well-dispersed GQDs were prepared with no further surface passivation process. Furthermore, the fluorescence of N-GQDs could be substantially quenched by Cu^{2+}, which could be explained by copper-induced self-quenching (Scheme 1).

Table 1. Comparison of the Proposed Methods with Other Methods

methods	starting material	time	emission	yield	reference
pyrolysis	trisodium citrate	4 min	420 nm	3.6%	34
hydrothermal	citric acid	5 h	440 nm	7.2%	35
microwave-assisted pyrolysis	aspartic acid and NH_4HCO_3	10 min	442 nm	14%	36
carbonization	citric acid	35 min	460 nm	9%	27
pyrolysis	tyrosine and glucose	1 min	522 nm	12%	this work

Scheme 1. Schematic Illustration of the Formation of N-GQDs and Their Response to Cu^{2+}

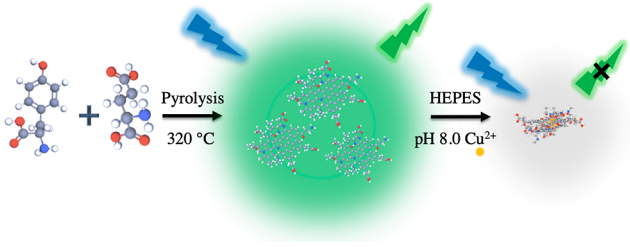

Characterization of N-GQDs. In Figure 1, the morphology and crystal form of the N-GQDs were characterized by

https://doi.org/10.1021/acsomega.3c02705
ACS Omega 2023, 8, 27333−27343

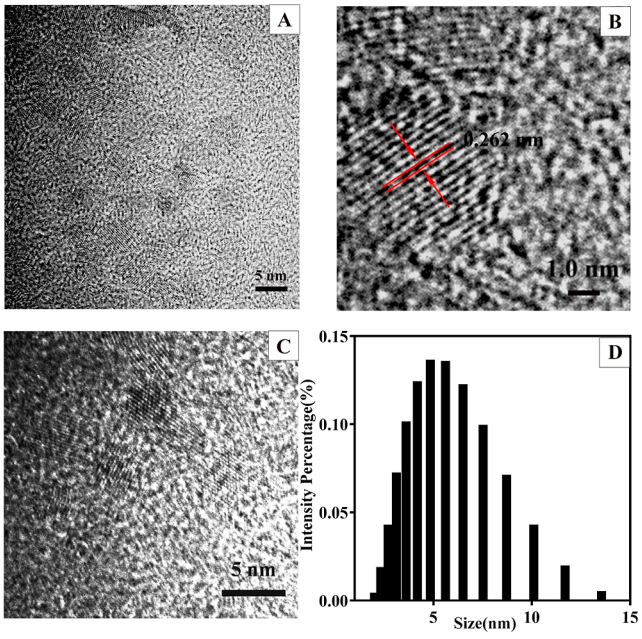

Figure 1. (a–c) HRTEM images of the N-GQDs (0.262 nm). (d) Size distribution of the N-GQDs obtained by DLS.

high-resolution transmission electron microscopy (HRTEM). The N-GQDs showed thin-film structures with fine monodispersity with an average diameter of 5.0 ± 1.3 nm, which was calculated from over 100 sheets in TEM images. The lattice spacing of the prepared N-GQDs was measured to be ca. 0.26 nm, which indicates the formation of the graphitic carbon.[37] The hydrodynamic diameter of N-GQDs was measured by DLS to be 5.1 ± 2.0 nm (Figure 1d), which was comparable with the results obtained from TEM.

A series of experiments have been performed to further investigate and confirm the structure of N-GQDs. The XRD patterns were used to validate the graphitic structure of the N-GQDs. As shown in Figure 2a, a broad peak was detected and centered at 2θ = 20°, which could be corresponding to the characteristic peak of the turbostratic carbon phase that matches with the XRD patterns reported in other N-GQDs.[38] XPS was conducted to detect the composition and surface functional groups in N-GQDs. There were three main peaks at 284.0, 530.4, and 399.2 eV which were attributed to C 1s, O 1s, and N 1s, respectively (Figure 2b). The atomic percentage of carbon, oxygen, and nitrogen was calculated to be ca. 61.4, 28.5, and 10.2%, respectively, which were the three main elements in the prepared GQDs. The C 1s spectrum of N-GQDs (Figure 2c) showed six peaks at 284.4, 285.1, 286.1, 287.8, 288.1, and 288.4 eV, indicating the presence of C═C, C−C/C−H, C−N/C−OH/═C−NH, C−O−C/N−C═O/−C═N$^+$, C═O, and −COOH, respectively. The N 1s spectrum of N-GQDs (Figure 2d) presented three peaks at 398.70, 399.40, and 400.35 eV, indicating the presence of pyridinic, pyrrolic, and graphitic N structure. All these data from XPS analysis suggested that the C, O, and N atoms were the major components in the N-GQDs.

In addition, Raman spectroscopy was used for further identifying the structure of the produced N-GQDs. As presented in Figure 3A, the spectroscopy showed two characteristic peaks at ca. 1434 and 1654 cm^{-1}, referring to the typical G bands caused by the vibration of the sp^2 hybridization of carbon and D bands attributable to the defect

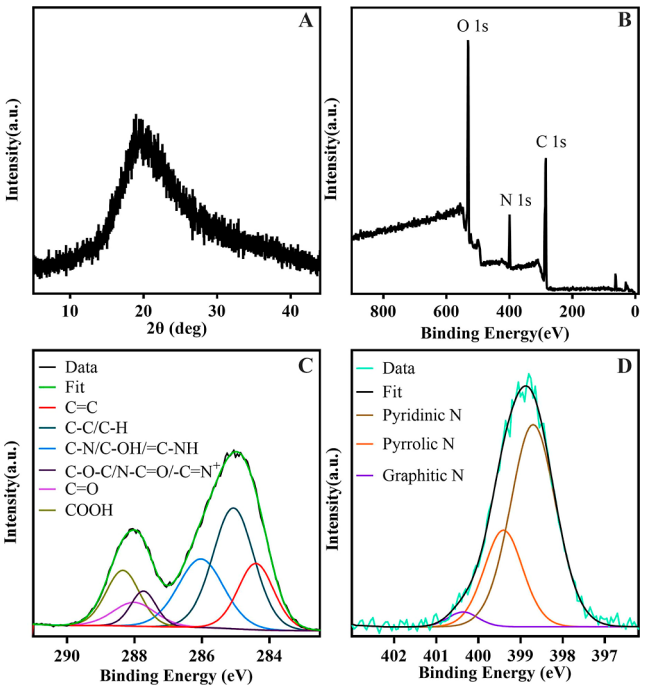

Figure 2. (a) XRD patterns of the GQDs. (b) Survey XPS spectra of the GQDs. (c) High-resolution C 1s spectra of the N-GQDs. (d) High-resolution N 1s spectra of the N-GQDs.

of the sp^2 network of N-GQDs.[39] Additionally, FTIR spectra were used to identify the structure variation of tyrosine and glutamic acid during the formation of N-GQDs in Figure 3B; comparing the curve of N-GQDs with glutamic acid and tyrosine, the peak area of N-GQDs that disappeared at ca. 3000 cm^{-1} indicated that C−H was vanished while the C═C stretching was formed, which proves the establishment of sp^2 hybridization of a carbon network at ca. 1500 cm^{-1}. Moreover, the C═C bending and stretching were found at ca. 850 and 1500 cm^{-1}. The broad peak from 3200 to 3500 cm^{-1} suggested the emergence of abundant O−H and N−H bonding, and the strong peak at 1676 cm^{-1} indicated the presence of C═O structures, which attributed to the existence of carboxylic groups and amides in N-GQDs. Additionally, the presence of N−O stretching was shown at 1550 cm^{-1}, and the presence of C−O and C−N stretching was found at ca. 1250 cm^{-1}. These active functional groups demonstrate the potential sites for surface modification.

Optical Properties of the GQDs. The optical properties of N-GQDs have been investigated to evaluate their potential in bioimaging. First, under the irradiation of 365 nm ultraviolet (UV) light, the N-GQDs showed strong green fluorescence, while the solution of glutamic acid and tyrosine showed no emission (Figure 4A), suggesting the formation of high-brightness fluorescent N-GQDs. Both UV−vis absorption and fluorescence spectra are shown in Figure 4B; the absorption of N-GQDs showed two obvious peaks in the UV region and a long tail expanding into the visible region. The first peak was shown at ca. 230 nm corresponding to the typical peak reported in other graphene oxide-based nanomaterials.[40] The second peak was exhibited at ca. 276 nm, attributing to the π to π^* transitions of aromatic C═C bonds.[41] There is a less obvious shoulder peak shown at ca. 323 nm, which could be considered as n to π^* transitions[42] in the oxygen or nitrogen functional groups of N-GQDs such as C═O, C−N, or C−O.

https://doi.org/10.1021/acsomega.3c02705
ACS Omega 2023, 8, 27333−27343

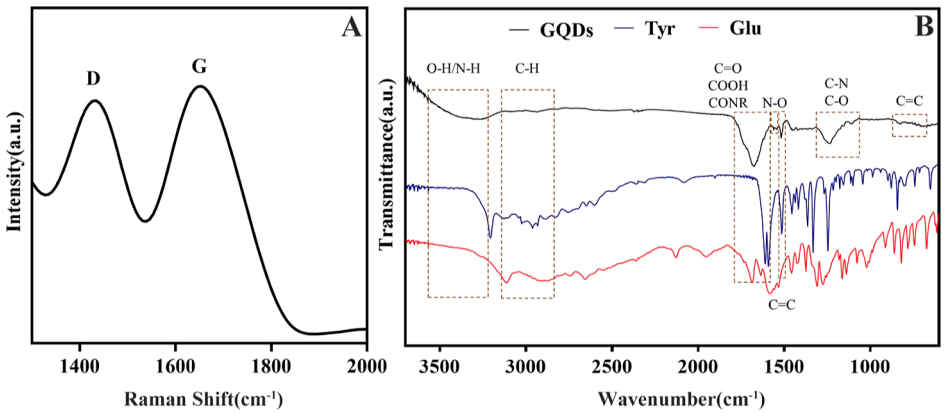

Figure 3. (A) Raman spectrum of the N-GQDs. (B) FTIR spectra of L-glutamic acid (red), tyrosine (blue), and N-GQDs (black).

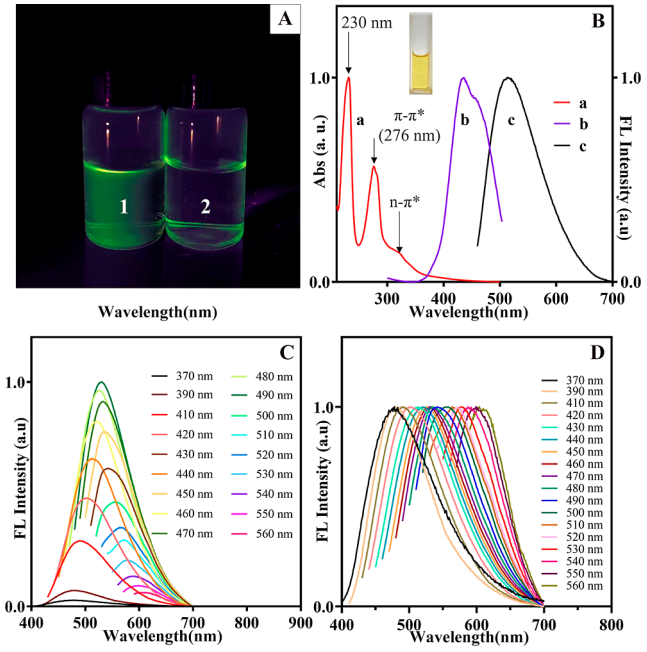

Figure 4. (A) Photographs of tyrosine and glutamic acid solution (2) and N-GQDs (1) excited under 365 nm UV light. (B) UV−vis absorption spectrum (curve a) and excitation (curve b) and emission spectra (curve c) of N-GQDs. λ_{ex} = 460 nm; λ_{em} = 522 nm. (C) Fluorescence emission spectra of N-GQDs with the excitation wavelength set from 370 to 560 nm. (D) Normalized spectra in (C).

A strong fluorescence peak appeared at 522 nm at an excitation wavelength of 460 nm. Moreover, the emission of N-GQDs exhibited a similar excitation-dependent behavior, and the emission peak shifted from 478 to 604 nm as the excitation wavelength varied from 370 to 560 nm.

Photostability and the pH Effect. The photostability and pH effect of N-GQDs were also investigated. As shown in Figure 5A, the fluorescence intensity of N-GQDs and FITC versus time curves were recorded. Both variation tendencies of the fluorescence intensity of N-GQDs and FITC decreased during the whole irradiation time, although there was mild fluorescence intensity enhancement, which could be attributed to the unstable intensity of the excitation laser during the long-time irradiation. In comparison with organic dyes like FITC, the fluorescence of N-GQDs showed superior capability against photobleaching. The fluorescence intensity of FITC was weakened about 40%, but the fluorescence intensity of N-GQDs was only quenched about 10% under the same irradiation time. This superior photostability offers the prepared N-GQDs possibilities in long-term bioimaging. Additionally, the effect of pH on the fluorescence intensity was also studied. The emission fluorescence intensity gradually increased as the pH increased until it reached to the highest value at pH 10, which demonstrates the excellent stability of N-GQDs in a high basic condition. The fluorescence intensity of N-GQDs is relatively high and stable from pH 5 to pH 9, which covers most of the physiological environment applications. The fluorescence intensity of N-GQDs started to reduce as the pH is over 10. Furthermore, the zeta potential of N-GQDs was also another discussion on stability. Figure 5C shows that the value varied from +3.43 to −22.8 mV as the pH enhanced from 3 to 12. The variation is due to the protonation and deprotonation of multiple functional groups such as carboxylic and amide groups. Those active functional groups could be associated with biomolecules, aptamers, or antibodies according to different purposes.

Fluorescence Stability of N-GQDs on Metal Ions. Besides the photostability and effects of pH, the impact of metal ions on fluorescence intensity has also been investigated. In Figure 6, it is shown that the fluorescence of N-GQDs could be significantly quenched by Cu^{2+} instead of other metal ions, which provide a new direction as a copper sensing probe. N-GQDs were incubated with each kind of metal ion at a concentration of 20 μM. The fluorescence intensity was significantly reduced after being mixed with Cu^{2+}, which could be explained by the chelating interactions of N-GQDs and Cu^{2+} to cause aggregation-induced self-quenching.

Feasibility Investigation of Cu^{2+} Detection. To further confirm the feasibility and mechanism of Cu^{2+} detection, the variation of absorption and fluorescence before and after adding Cu^{2+} was compared and is shown in Figure 7A,B. In the absorption spectrum of N-GQDs (black), the peak showed a strong absorption at ca. 230 nm, which confirmed the structure. After the addition of Cu^{2+}, the absorption peak was significantly reduced. Figure 7B shows that the aggregation-induced self-quenching reduced 61% intensity of N-GQDs in the presence of Cu^{2+}. Therefore, the detection mechanism of N-GQDs could be explained by the aggregation-induced self-quenching. We also compared the aggregated N-GQDs with well-dispersed N-GQDs in the HRTEM images. In Figure 7C, the images of N-GQDs without the addition of Cu^{2+} showed a well-dispersed single layer, but a significant aggregation was observed after the addition of Cu^{2+} as shown

https://doi.org/10.1021/acsomega.3c02705
ACS Omega 2023, 8, 27333−27343

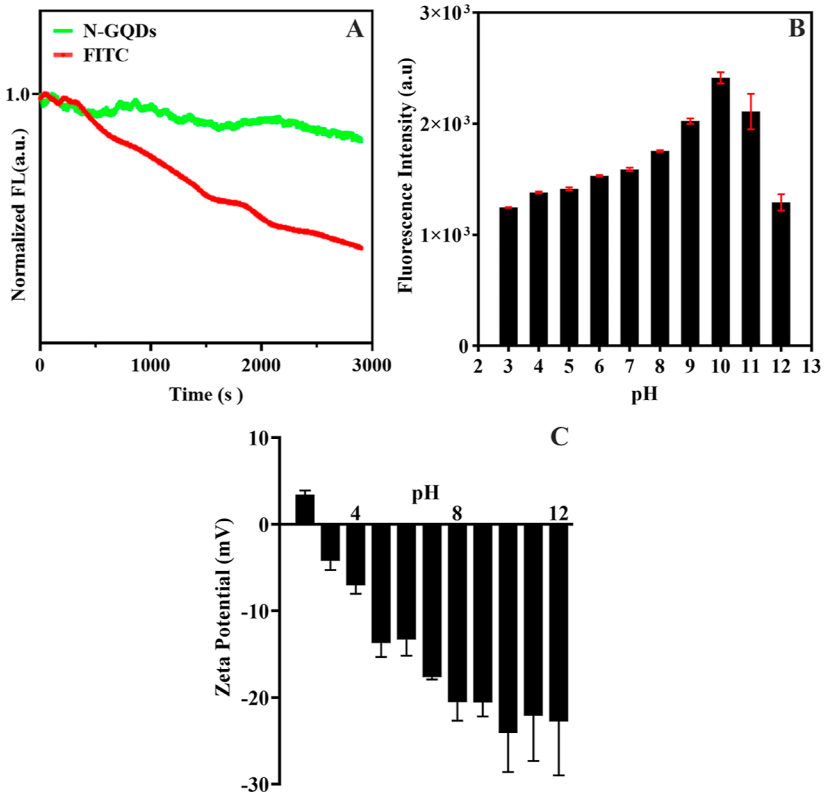

Figure 5. (A) Photostability of N-GQDs. (B) Effect of pH on the fluorescence intensity of N-GQDs. (C) Zeta potential of N-GQDs in different pH solutions.

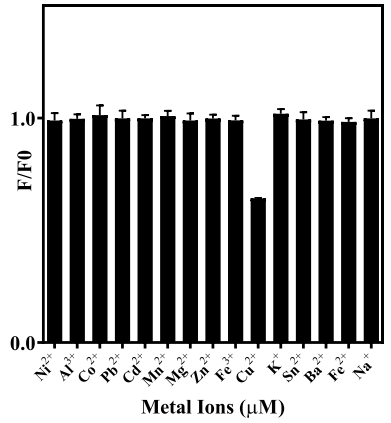

Figure 6. Effects of Cu^{2+} (20 μM) and other metal ions (20 μM) on the fluorescence intensity ratio of F/F_0. F and F_0 refer to the fluorescence intensity of N-GQDs with and without the addition of each metal ion, respectively. λ_{ex} = 460 nm and λ_{em} = 522 nm.

in Figure 7d, which confirmed the proposed theory of aggregation-induced fluorescence quenching in Scheme 1.

Detection of Cu^{2+}. The optimal conditions were investigated in three perspectives, including the concentration of N-GQDs, pH, and reaction time. First, the reaction time needs to be optimized first to ensure that the reaction is completed. Figure 8A shows that the treatment of N-GQDs and Cu^{2+} was controlled under different reaction times, and the fluorescence intensity was recorded as F. The concentration of N-GQDs in the control group with no Cu^{2+} was recorded as F_0. The ratio of F to F_0 could be used to evaluate the reaction process. In the beginning, it decreased fast, indicating that the reaction is happening. After 15 min, the slope gradually

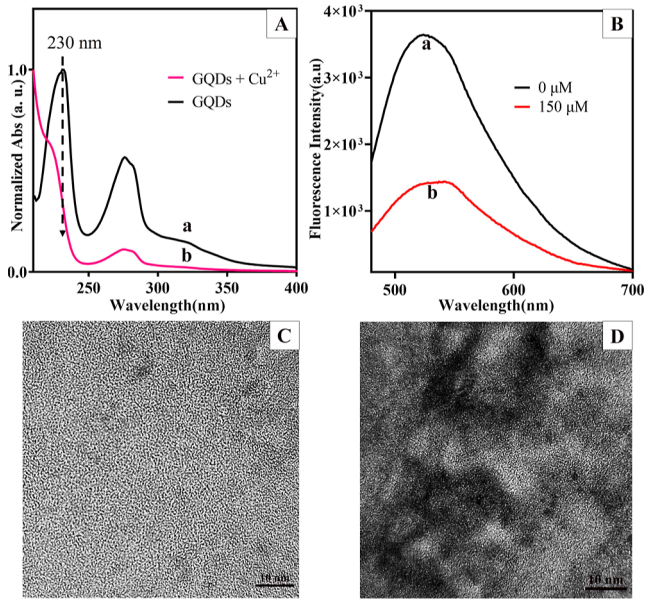

Figure 7. (A) Absorption spectra of N-GQDs (black) and N-GQDs added with Cu^{2+} (red). (B) Fluorescence spectra of N-GQDs (black) and N-GQDs added with Cu^{2+} (red). (C) HRTEM images of the N-GQDs in the absence of Cu^{2+} (0 μM). (D) HRTEM images of the N-GQDs in the presence of Cu^{2+} (150 μM).

reached plateau, indicating that the reaction between Cu^{2+} and N-GQDs was finished. Therefore, the reaction time was fixed down to 15 min for the following experiments. Second, the concentrations of N-GQDs were also a critical factor to influence the sensitivity; a series of different concentrations of N-GQDs were mixed with 40 μM Cu^{2+} in 20 mM HEPES at

https://doi.org/10.1021/acsomega.3c02705
ACS Omega 2023, 8, 27333−27343

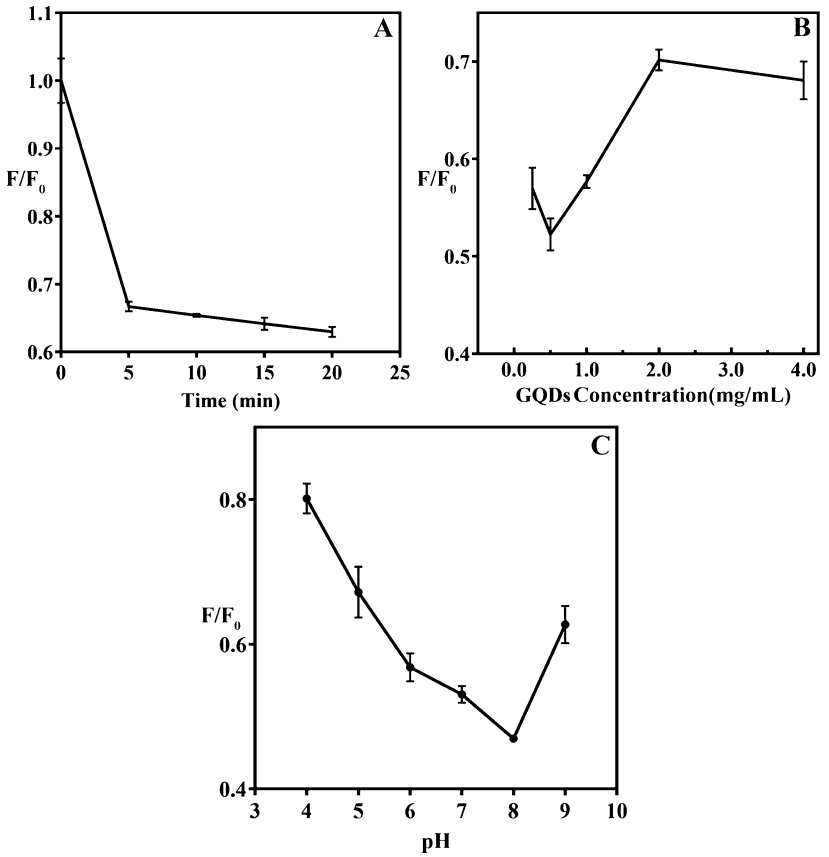

Figure 8. Condition optimization of selective detection of Cu^{2+}. (A) Reaction time, (B) concentration of N-GQDs, and (C) pH. F and F_0 refer to the fluorescence intensity of N-GQDs with and without the addition of Cu^{2+}, respectively. λ_{ex} = 460 nm and λ_{em} = 522 nm.

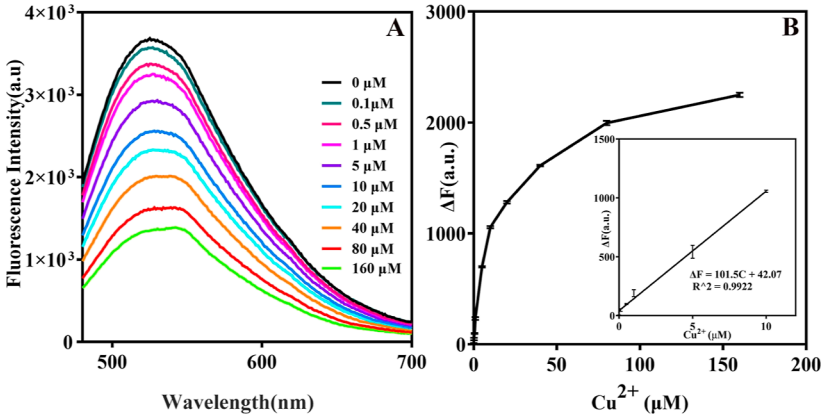

Figure 9. (A) Fluorescence spectra of N-GQDs incubated with different concentrations of Cu^{2+} in 20 mM HEPES (pH 8.0). (B) Plot of the fluorescence intensity variation ΔF vs the concentrations of Cu^{2+}. The inset graph in (B) showed the calibration curve of the N-GQDs for Cu^{2+} detection. λ_{ex} = 460 nm and λ_{em} = 522 nm. F_0 and F represent the fluorescence intensity of GQDs in the absence and presence of Cu^{2+}, respectively.

pH 7. In Figure 8B, the ratio (F/F_0) showed a minimum value at a concentration of 0.5 mg/mL of GQDs, which is the optimal concentration of N-GQDs to detect Cu^{2+}.

Third, the fluorescence intensity of these newly prepared N-GQDs was influence by pH; therefore, as a newly developed copper sensing fluorescent probe, the pH condition of each measurement was required to be seriously controlled, which means that all the experiments were performed under one optimal condition. In this project, HEPES buffer was used to seriously control the pH condition under each measurement. Based on the mechanism of this GQD-based copper sensor, their chelating interactions with Cu^{2+} led to the aggregation and significant fluorescence quenching. The optimal pH condition should cause the highest fluorescence intensity variation, corresponding to the strongest energy transfer. The optimal pH was investigated by mixing N-GQDs and Cu^{2+} in a series of different pH conditions. The best detection performance was at pH 8. Accordingly, pH 8 was chosen as the optimal pH for analysis.

In summary, the developed N-GQDs could be used to selectively detect Cu^{2+} under the optimized conditions (0.50 mg/mL in 20 mM HEPES buffer, pH = 8.0, and 15 min reaction time). As shown in Figure 9A, the fluorescence

https://doi.org/10.1021/acsomega.3c02705
ACS Omega 2023, 8, 27333−27343

intensity of N-GQDs decreased as the concentration of Cu^{2+} enhanced.

The fluorescence variation showed a concentration-reliant manner, which is shown in Figure 9B. The curve showed the relationship between the fluorescence variation ($\Delta F = F_0 - F$) and the concentration of Cu^{2+} (F_0 and F represent the fluorescence intensity of N-GQDs in the absence and presence of Cu^{2+}, respectively). The dynamic range of the N-GQD-based copper sensor was from 0 to 160 μM with the linear range from 0.1 to 10 μM (inset of Figure 9B). The calibration curve showed a linear regression with the equation ΔF = 101.5C + 42.07 and a correlation coefficient of 0.9926, where C represents the concentration of Cu^{2+}. The limit of detection (LOD) for selective detection of Cu^{2+} was calculated to be 60 nM based on the slope of the equation ($3\sigma/s$), where σ is the standard deviation of three blank signals and s is the slope of the calibration curve. Table 2 shows the comparison of this work with other methods, and the detection limit of this N-GQD-based sensing system of Cu^{2+} is lower than the reported methods (Table 2), which could be explained by the excellent chelating efficiency between carboxyl-functionalized N-GQDs and divalent copper cations. Therefore, compared with other divalent copper cation sensing probes, the prepared N-GQDs were fabricated with two natural amino acids with a low-cost superficial synthesis method, which could be applied in Cu^{2+} detection in an aqueous environment.

Table 2. Comparison of the Proposed Fluorometric Method on Divalent Copper Cations with Other Methods

sensing target	LOD	linear range	method	references
Au nanoparticles	1.52 μM	2−468 μM	colorimetric	43
silver nanoclusters	0.71 μM	0−28 μM	fluorometric	44
polymer nanoparticles	0.577 μM	0−100 μM	fluorometric	45
GQDs	0.226 μM	0−15 μM	fluorometric	46
this work	0.06 μM	0.1−10 μM	fluorometric	this work

In Vitro Fluorescence Imaging and Copper Ion Effect in Cell Imaging. Previous experiments demonstrated the superior fluorescence properties of the prepared N-GQDs. Therefore, the N-GQDs were further evaluated in vitro. One cancer cell line and one normal cell line, including mouse leukemic macrophage cell line (RAW 264.7) and human embryonal kidney cell line (293FT), were chosen for their fast growing and easy proliferation. First, the biocompatibility of the N-GQDs was tested. As discussed in the experimental part, the MTT assay was performed to investigate the toxicity of N-GQDs after being incubated for 24 h. In Figure 10, both cell lines showed high viability from the highest concentration of 10.0 mg/mL to the lowest concentration of 0.01 μg/mL. There was no significant difference between the control and other treated groups (*p < 0.05), suggesting superior biocompatibility.

The excellent biocompatibility ensures N-GQDs their potential for in vitro applications. Given that the previous experiments confirmed this sensing system's feasibility in an aqueous buffer environment, we expanded and continued to test feasibility in the cell environment. The prepared N-GQDs were incubated with RAW 264.7 cells in 10 mM PBS buffer to introduce them via endocytosis. Meanwhile, copper ions were added under the same condition. After incubation for 1 h, the cells were washed with PBS buffer to remove free N-GQDs left on the cell surface. In Figure 11A, the cells stained with DAPI confirmed the cell position (strong blue fluorescence). The green color spot localized in the cells is the fluorescence signal of N-GQDs, which emitted strong green on excitation at 458 nm. The confocal fluorescence images of RAW 264.7 cells with the addition of different concentrations of Cu^{2+} are presented in different columns, respectively. With the concentrations of Cu^{2+} enhanced, the fluorescence of N-GQD intensity reduced, indicating the potential of monitoring intracellular Cu^{2+} level variations in cells. Besides, the fluorescence images without Cu^{2+} treatment demonstrated that N-GQDs easily penetrate the cells through endocytosis and emit strong fluorescence to serve as fluorescence imaging agents. In Figure 11B, the fluorescence intensities of N-GQDs in the images were quantitatively measured, and the fluorescence intensity in cells decreased as the concentration of Cu^{2+} enhanced from 0 to 200 μM, indicating the potential to monitor the Cu^{2+} level in cells.

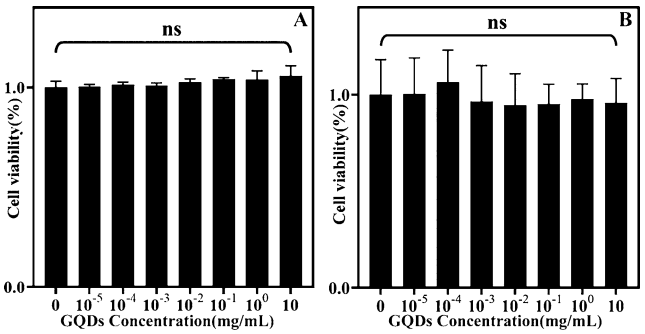

Figure 10. Cell viability of RAW 264.7 cells (A) and 293FT cells (B) after being treated with different concentrations of N-GQDs for 24 h.

Application in a Diluted Serum Sample. To evaluate the feasibility of N-GQDs in a serum environment, FBS samples were first spiked with two different concentrations of Cu^{2+} (4 and 8 μM) and then detected by fluorometry and graphite furnace atomic absorption spectroscopy. The spike recovery results from these two methods are shown in Table 3. Both the fluorometric and GFAAS methods showed decent recoveries; the recoveries of all samples from the fluorometric assay were 101 and 102% at those two different concentrations, respectively, suggesting that these newly developed N-GQDs have the potential for the detection of Cu^{2+} in living cells. Besides, compared with the GFAAS method, the fluorometric method is fast to detection and easy to operate.

CONCLUSIONS

In summary, we have fabricated strong green emission N-GQDs with glutamic acid and tyrosine as the carbon source under one-pot synthesis. The prepared N-GQDs showed superior photostability and biocompatibility to serve as bioimaging agents. Moreover, the fluorescence signal of these newly developed N-GQDs was proportional to the concentration of Cu^{2+}, which could be explained by chelation-induced fluorescence quenching between carboxylic groups and Cu^{2+}. The sensing probe showed the linear range from 0.1 to 10 μM Cu^{2+} and a LOD of 60 nM. Compared with other GQD-based copper sensors, the routine of these newly developed GQDs was fast and superficial. Instead of using some expensive organic complicated precursors, this method chose two amino acids. This simple and low-technique method was suitable for large-scale production for commercialization. In addition, the

https://doi.org/10.1021/acsomega.3c02705
ACS Omega 2023, 8, 27333−27343

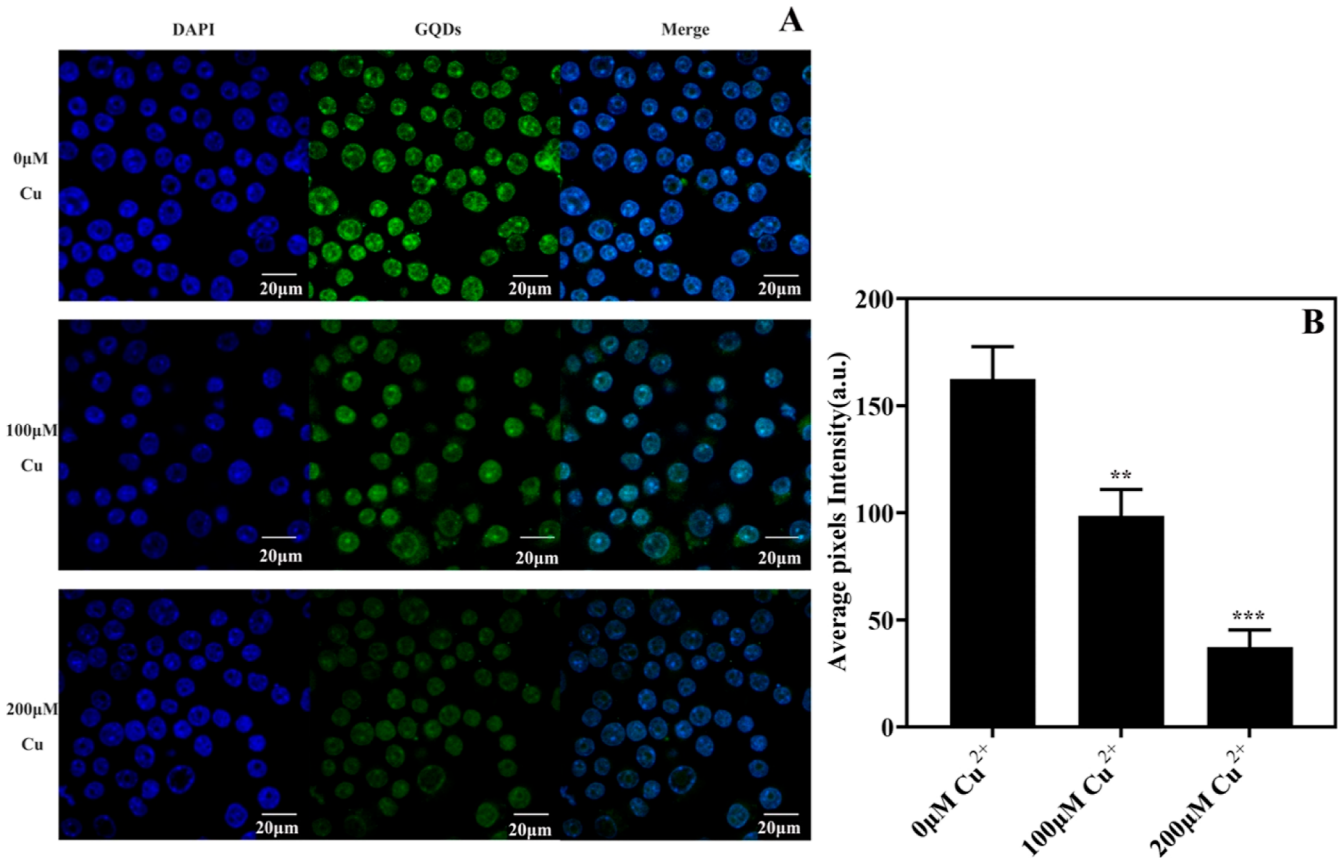

Figure 11. (A) Confocal fluorescence images of RAW 264.7 cells incubated with N-GQDs at different concentrations of Cu^{2+}, including 0, 100, and 200 μM. The nucleus was counterstained with DAPI (blue). The green fluorescence was from N-GQDs. (B) The fluorescence intensity of N-GQDs in cells was quantified by ImageJ software. (***$p < 0.001$ and **$p < 0.01$).

Table 3. Spike Recovery Level of GFAAS and Fluorometric Methods for Cu^{2+} Detection in FBS (n = 3)

methods	samples	spiked	detected	recovery of this method (%)
fluorometric	FBS	4.0 μM	4.03 ± 0.19 (μM)	101 ± 4.7
	FBS	8.0 μM	7.93 ± 1.07 (μM)	102 ± 4.9
GFAAS	FBS	4.0 μM	4.17 ± 0.21 (μM)	104 ± 5.3
	FBS	8.0 μM	7.91 ± 0.21 (μM)	99 ± 2.6

N-GQDs also showed significant fluorescence response to Cu^{2+} in serum and living cells, demonstrating their potential to apply in biomedical studies.

AUTHOR INFORMATION

Corresponding Author

Bingxue Sun − *Department of pharmacy, Jilin University, Changchun, Jilin 130012, China*; Email: sunbingxue@jlu.edu.cn

Author

Xiao Liu − *Department of pharmacy, Jilin University, Changchun, Jilin 130012, China*; orcid.org/0000-0002-8704-6102

Complete contact information is available at: https://pubs.acs.org/10.1021/acsomega.3c02705

Author Contributions

The manuscript was written through contributions of all authors. All authors have given approval to the final version of the manuscript.

Notes

The authors declare no competing financial interest.

ACKNOWLEDGMENTS

This work was supported by the Overseas PhD Science Foundation from Jilin University. The authors acknowledge the use of all the platform test facilities provided by Jilin University.

REFERENCES

(1) Biswas, M. C.; Islam, M. T.; Nandy, P. K.; Hossain, M. M. Graphene quantum dots (GQDs) for bioimaging and drug delivery applications: A review. *ACS Mater. Lett.* **2021**, *3*, 889−911.

(2) Tian, P.; Tang, L.; Teng, K. S.; Lau, S. P. Graphene quantum dots from chemistry to applications. *Mater. Today Chem.* **2018**, *10*, 221−258.

(3) Younis, M. R.; He, G.; Lin, J.; Huang, P. Recent advances on graphene quantum dots for bioimaging applications. *Front. Chem.* **2020**, *8*, 424.

(4) Zhao, C.; Song, X.; Liu, Y.; Fu, Y.; Ye, L.; Wang, N.; Wang, F.; Li, L.; Mohammadniaei, M.; Zhang, M.; Zhang, Q.; Liu, J. Synthesis of graphene quantum dots and their applications in drug delivery. *J. Nanobiotechnol.* **2020**, *18*, 142.

(5) Kumar, Y. R.; Deshmukh, K.; Sadasivuni, K. K.; Pasha, S. K. K. Graphene quantum dot based materials for sensing, bio-imaging and

https://doi.org/10.1021/acsomega.3c02705
ACS Omega 2023, 8, 27333−27343

energy storage applications: A review. *RSC Adv.* **2020**, *10*, 23861−23898.
(6) Chung, S.; Revia, R. A.; Zhang, M. Graphene quantum dots and their applications in bioimaging, biosensing, and therapy. *Adv. Mater.* **2021**, *33*, 1904362.
(7) Tkaczyk, A.; Mitrowska, K.; Posyniak, A. Synthetic organic dyes as contaminants of the aquatic environment and their implications for ecosystems: A review. *Sci. Total Environ.* **2020**, *717*, 137222.
(8) Alford, R.; Simpson, H. M.; Duberman, J.; Hill, G. C.; Ogawa, M.; Regino, C.; Kobayashi, H.; Choyke, P. L. Toxicity of organic fluorophores used in molecular imaging: Literature review. *Mol. Imaging* **2009**, *8*, 341−354.
(9) García de Arquer, F. P.; Talapin, D. V.; Klimov, V. I.; Arakawa, Y.; Bayer, M.; Sargent, E. H. Semiconductor quantum dots: Technological progress and future challenges. *Science* **2021**, *373*, 640.
(10) Valizadeh, A.; Mikaeili, H.; Samiei, M.; Farkhani, S. M.; Zarghami, N.; kouhi, M.; Akbarzadeh, A.; Davaran, S. Quantum dots: Synthesis, bioapplications, and toxicity. *Nanoscale Res. Lett.* **2012**, *7*, 480.
(11) Thangadurai, T. D.; Manjubaashini, N.; Nataraj, D.; Gomes, V.; Lee, Y. I. A review on graphene quantum dots, an emerging luminescent carbon nanolights: Healthcare and environmental applications. *Mater. Sci. Eng. B* **2022**, *278*, 115633.
(12) Ghaffarkhah, A.; Hosseini, E.; Kamkar, M.; Sehat, A. A.; Dordanihaghighi, S.; Allahbakhsh, A.; Kuur, C.; Arjmand, M. Synthesis, applications, and prospects of graphene quantum dots: A comprehensive review. *Small* **2022**, *18*, 2102683.
(13) Zhu, S.; Song, Y.; Wang, J.; Wan, H.; Zhang, Y.; Ning, Y.; Yang, B. Photoluminescence mechanism in graphene quantum dots: Quantum confinement effect and surface/edge state. *Nano Today* **2017**, *13*, 10−14.
(14) Li, M.; Chen, T.; Gooding, J. J.; Liu, J. Review of carbon and graphene quantum dots for sensing. *ACS Sens.* **2019**, *4*, 1732−1748.
(15) Chen, W.; Lv, G.; Hu, W.; Li, D.; Chen, S.; Dai, Z. Synthesis and applications of graphene quantum dots: A review. *Nanotechnol. Rev.* **2018**, *7*, 157−185.
(16) Kalluri, A.; Debnath, D.; Dharmadhikari, B.; Patra, P. Chapter Twelve—Graphene Quantum Dots: Synthesis and Applications. *Enzyme Nanoarchitectures: Enzymes Armored with Graphene*; Kumar, C. V., Ed.; Academic Press, 2018; Vol. *609*, pp 335−354.
(17) Kadyan, P.; Malik, R.; Bhatia, S.; Al Harrasi, A.; Mohan, S.; Yadav, M.; Dalal, S.; Ramniwas, S.; Kumar Kataria, S.; Arasu, T. Comprehensive review on synthesis, applications, and challenges of graphene quantum dots (GQDs). *J. Nanomater.* **2023**, *2023*, 1−26.
(18) Al-jahdaly, B.; Elsadek, M. F.; Ahmed, B.; Farahat, M. F.; Taher, M.; Khalil, A. Outstanding graphene quantum dots from carbon source for biomedical and corrosion inhibition applications: A review. *Sustainability* **2021**, *13*, 2127.
(19) Fu, Y.; Gao, G.; Zhi, J. Electrochemical synthesis of multicolor fluorescent N-doped graphene quantum dots as a ferric ion sensor and their application in bioimaging. *J. Mater. Chem. B* **2019**, *7*, 1494−1502.
(20) Xie, J.-D.; Lai, G.-W.; Huq, M. Hydrothermal route to graphene quantum dots: Effects of precursor and temperature. *Diamond Relat. Mater.* **2017**, *79*, 112−118.
(21) Kang, C.; Huang, Y.; Yang, H.; Yan, X.-F.; Chen, Z.-P. A review of carbon dots produced from biomass wastes. *Nanomaterials* **2020**, *10*, 2316.
(22) Liu, R.; Wu, D.; Feng, X.; Müllen, K. Bottom-up fabrication of photoluminescent graphene quantum dots with uniform Morphology. *J. Am. Chem. Soc.* **2011**, *133*, 15221−15223.
(23) Huang, D.; Zhou, H.; Wu, Y.; Wang, T.; Sun, L.; Gao, P.; Sun, Y.; Huang, H.; Zhou, G.; Hu, J. Bottom up synthesis and structural design strategy for graphene quantum dots with tunable emission to the near infrared region. *Carbon* **2019**, *142*, 673−684.
(24) Liu, Z.; Fu, S.; Liu, X.; Narita, A.; Samorì, P.; Bonn, M.; Wang, H. I. Small size, big impact: Recent progress in bottom up synthesized nanographenes for optoelectronic and energy applications. *Adv. Sci.* **2022**, *9*, 2106055.
(25) Atienzar, P.; Primo, A.; Lavorato, C.; Molinari, R.; García, H. Preparation of graphene quantum dots from pyrolyzed alginate. *Langmuir* **2013**, *29*, 6141−6146.
(26) Naik, J. P.; Sutradhar, P.; Saha, M. Molecular scale rapid synthesis of graphene quantum dots (GQDs). *J. Nanostructure Chem.* **2017**, *7*, 85−89.
(27) Dong, Y.; Shao, J.; Chen, C.; Li, H.; Wang, R.; Chi, Y.; Lin, X.; Chen, G. Blue luminescent graphene quantum dots and graphene oxide prepared by tuning the carbonization degree of citric acid. *Carbon* **2012**, *50*, 4738−4743.
(28) Ngoc Anh, N. T.; Chang, P.-Y.; Doong, R.-A. Sulfur-doped graphene quantum dot-based paper sensor for highly sensitive and selective detection of 4-nitrophenol in contaminated water and wastewater. *RSC Adv.* **2019**, *9*, 26588−26597.
(29) Tajik, S.; Dourandish, Z.; Zhang, K.; Beitollahi, H.; Le, Q. V.; Jang, H. W.; Shokouhimehr, M. Carbon and graphene quantum dots: a review on syntheses, characterization, biological and sensing applications for neurotransmitter determination. *RSC Adv.* **2020**, *10*, 15406−15429.
(30) Sohal, N.; Maity, B.; Basu, S. Recent advances in heteroatom-doped graphene quantum dots for sensing applications. *RSC Adv.* **2021**, *11*, 25586−25615.
(31) Qu, D.; Zheng, M.; Du, P.; Zhou, Y.; Zhang, L.; Li, D.; Tan, H.; Zhao, Z.; Xie, Z.; Sun, Z. Highly luminescent S, N co-doped graphene quantum dots with broad visible absorption bands for visible light photocatalysts. *Nanoscale* **2013**, *5*, 12272−12277.
(32) Shi, W.; Fan, H.; Ai, S.; Zhu, L. J. N. J. o. C. Preparation of fluorescent graphene quantum dots from humic acid for bioimaging application. *New J. Chem.* **2015**, *39*, 7054−7059.
(33) Feng, J.; Dong, H.; Pang, B.; Shao, F.; Zhang, C.; Yu, L.; Dong, L. Theoretical study on the optical and electronic properties of graphene quantum dots doped with heteroatoms. *Phys. Chem. Chem. Phys.* **2018**, *20*, 15244−15252.
(34) Hong, G.-L.; Zhao, H.-L.; Deng, H.-H.; Yang, H.-J.; Peng, H. P.; Liu, Y.-H.; Chen, W. Fabrication of ultra-small monolayer graphene quantum dots by pyrolysis of trisodium citrate for fluorescent cell imaging. *Int. J. Nanomed.* **2018**, *13*, 4807−4815.
(35) Dhenadhayalan, N.; Lin, K.-C.; Suresh, R.; Ramamurthy, P. Unravelling the Multiple Emissive States in Citric-Acid-Derived Carbon Dots. *J. Phys. Chem. C* **2016**, *120*, 1252−1261.
(36) Zhang, C.; Cui, Y.; Song, L.; Liu, X.; Hu, Z. Microwave assisted one-pot synthesis of graphene quantum dots as highly sensitive fluorescent probes for detection of iron ions and pH value. *Talanta* **2016**, *150*, 54−60.
(37) Yang, L.; Qin, A.; Chen, S.; Liao, L.; Qin, J.; Zhang, K. Manganese(II) enhanced fluorescent nitrogen-doped graphene quantum dots: a facile and efficient synthesis and their applications for bioimaging and detection of Hg^{2+} ions. *RSC Adv.* **2018**, *8*, 5902−5911.
(38) Parvizi, R.; Azad, S.; Dashtian, K.; Ghaedi, M.; Heidari, H. Natural source-based graphene as sensitising agents for air quality monitoring. *Sci. Rep.* **2019**, *9*, 3798.
(39) Chhabra, V. A.; Kaur, R.; Kumar, N.; Deep, A.; Rajesh, C.; Kim, K.-H. Synthesis and spectroscopic studies of functionalized graphene quantum dots with diverse fluorescence characteristics. *RSC Adv.* **2018**, *8*, 11446−11454.
(40) Wazir, A. H.; Kundi, I. W. Synthesis of graphene nano sheets by the rapid reduction of electrochemically exfoliated graphene oxide induced by microwaves. *J. Chem. Soc. Pak.* **2016**, *38*, 11−16.
(41) Rajender, G.; Giri, P. K.; Rajender, G.; Giri, P. K. Formation mechanism of graphene quantum dots and their edge state conversion probed by photoluminescence and Raman spectroscopy. *J. Mater. Chem. C* **2016**, *4*, 10852−10865.
(42) Novoa-De León, I. C.; Johny, J.; Vázquez-Rodríguez, S.; García-Gómez, N.; Carranza-Bernal, S.; Mendivil, I.; Shaji, S.; Sepúlveda-Guzmán, S. Tuning the luminescence of nitrogen-doped graphene quantum dots synthesized by pulsed laser ablation in liquid and their use as a selective photoluminescence on−off−on probe for ascorbic acid detection. *Carbon* **2019**, *150*, 455−464.

https://doi.org/10.1021/acsomega.3c02705
ACS Omega 2023, 8, 27333−27343

(43) Chang, C.-C.; Lee, C.-H.; Wu, T.-H.; Chen, C.-P.; Chen, C.-Y.; Lin, C.-W. Reversion of gold nanoparticle aggregates for the detection of Cu^{2+} and its application in immunoassays. *Analyst* **2017**, *142*, 4684−4690.
(44) Yang, T.; Xie, Y.; Zhang, S.; He, X. Synthesis of dual red-emitting fluorescent silver nanoclusters in aqueous lipoic acid-based polymer solutions and application for Cu^{2+} detection and cell imaging. *ChemistrySelect* **2022**, *7*, No. e202200185.
(45) Luo, F.; Zhu, M.; Liu, Y.; Sun, J.; Gao, F. Ratiometric and visual determination of copper ions with fluorescent nanohybrids of semiconducting polymer nanoparticles and carbon dots. *Spectrochim. Acta, Part A* **2023**, *295*, 122574.
(46) Wang, F.; Gu, Z.; Lei, W.; Wang, W.; Xia, X.; Hao, Q. Graphene quantum dots as a fluorescent sensing platform for highly efficient detection of copper (II) ions. *Sens. Actuators, B* **2014**, *190*, 516−522.

https://doi.org/10.1021/acsomega.3c02705
ACS Omega 2023, 8, 27333−27343